LA-UR- 99-1054

Approved for public release;
distribution is unlimited.

Title: ANALYSIS AND SYSTEM DESIGN FRAMEWORK FOR INFRARED SPATIAL HETERODYNE SPECTROMETERS

Author(s): Bradly J. Cooke, Barham W. Smith, Bryan E. Laubscher, Pierre V. Villeneuve, and Scott D. Briles

Submitted to: SPIE AeroSense, Infrared Imaging Systems: Design, Analysis, and Testing X, April 5-9, 1999, Marriott World Center, Orlando, FL

Los Alamos
NATIONAL LABORATORY

DISCLAIMER

DISCLAIMER

Portions of this document may be illegible in electronic image products. Images are produced from the best available original document.

Analysis and System Design Framework for Infrared Spatial Heterodyne Spectrometers

Bradly J. Cooke, Barham W. Smith, Bryan E. Laubscher,
Pierre V. Villeneuve, and Scott Briles

Los Alamos National Laboratory
MS-D448, P.O. Box 1663
Los Alamos, New Mexico 87545
505-667-8512

ABSTRACT

We present a preliminary analysis and design framework developed for the evaluation and optimization of infrared, Imaging Spatial Heterodyne Spectrometer (SHS) electro-optic systems. Commensurate with conventional interferometric spectrometers, SHS modeling requires an integrated analysis environment for rigorous evaluation of system error propagation due to detection process, detection noise, system motion, retrieval algorithm and calibration algorithm. The analysis tools provide for optimization of critical system parameters and components including: i) optical aperture, f-number, and spectral transmission, ii) SHS interferometer grating and Littrow parameters, and iii) image plane requirements as well as cold shield, optical filtering, and focal-plane dimensions, pixel dimensions and quantum efficiency, iv) SHS spatial and temporal sampling parameters, and v) retrieval and calibration algorithm issues.

Keywords: Infrared Fourier Transform Spectroscopy, Spatially Modulated FTS

1.0 INTRODUCTION

The basic function of an infrared imaging Fourier Transform Spectrometer (FTS) is the capture and generation, through optical collection and electro-optical conversion, of a hyperspectral facsimile of the radiated and reflected infrared electromagnetic energy emanating from an extended scene. The resulting PxQxN hyperspectral data cube consists of two (image) spatial dimensions by N spectral dimensions. The PxQ spatial resolution of the data cube is determined by the system optical transfer function (OTF), while the spectral resolution is related to the Fourier transformed intensity distribution induced by the path-differenced, two-beam wavefront interference of the image. As will be discussed in this paper, the imaging Spatial Heterodyne Spectrometer[1,2] (SHS) employs a novel pushbroomed optical grating based concept for the acquisition of the PxQxN data cube. What immediately follows, is a brief review of wavefront interference as applied to transform spectrometers and a qualitative summary of basic imaging FTS concepts leading up to the Spatial Heterodyne Spectrometer.

The interference of two mutually identical wavefronts, $\mathbf{k}_1 = \mathbf{k}_2$, at the image plane is schematically diagrammed in **Figure 1**. As the focal plane array (FPA) pixels follow

A) Wavefront Interference

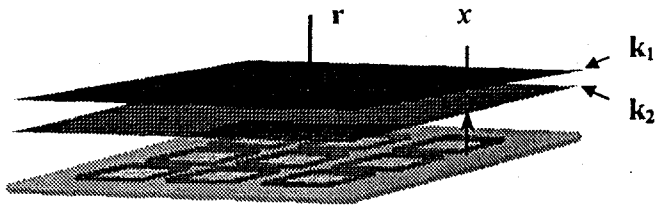

Focal Plane Array

B) Interferogram - Intensity Distribution

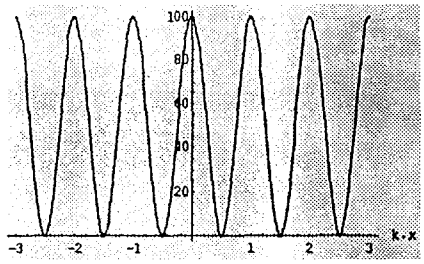

C) Interferogram - Fringe Pattern

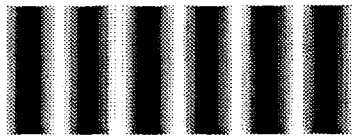

$$\Phi(\mathbf{r}) = |\mathbf{k}_1|^2 + |\mathbf{k}_2|^2 + 2\sqrt{|\mathbf{k}_1||\mathbf{k}_2|}\cos\left(\left(\frac{\mathbf{k}_1}{|\mathbf{k}_1|} - \frac{\mathbf{k}_2}{|\mathbf{k}_2|}\right)\cdot\mathbf{r}\right)$$

$$\Rightarrow \Phi(x) \propto 2I_o[1+\cos(2\pi k x)], \quad for\ \mathbf{k} = \mathbf{k}_1 = \mathbf{k}_2,\ I_o = |\mathbf{k}|^2$$

Figure 1. A) Wavefront interference of two identical beams at the image plane. **B)** Detected interferogram intensity distribution for k = constant and $kx = \pm 3$, and **C)** fringe pattern. Of importance, the wavenumber and intereferogram are related through the Fourier (Cosine) transform.

modulus-squared detection principles[3], the interference of the two fields results in an intensity[4] modulation related to the wavefronts relative path difference, x, and wavenumber, k, through

$$\Phi(x,k) \propto 1+\cos(2\pi k x). \qquad [1]$$

By sweeping the relative wavefront path difference, x, through an appropriate range, an interferogram in the form of a density distribution or fringe pattern may be generated and sampled. Through superposition principles, the single wavenumber, k, of **Equation 1** may be replaced by a weighted spectrum, $S(k)$, resulting in

$$\Phi(x) \propto \int_k S(k)(1+\cos(2\pi k x))dk\,, \qquad [2]$$

with $S(k)$ and interferogram $\Phi(x)$ uniquely related through the Fourier (cosine) transform.

Application of wavefront interference to imaging transform spectroscopy is demonstrated in **Figure 2**. The basic Michelson[5] imaging spectrometer consists of an optical filter, interferometer, and a focal plane array. Shown in its simplest form (two mirrors and a beamsplitter), the interferometer splits the image into two beams, which are recombined at the image plane with a relative path difference, δx, introduced by the movable mirror. By sweeping the movable mirror over a prescribed travel distance, $\pm\Delta x$, the interferogram at each image point is sequentially sampled at the FPA. Inversion of the interferogram through **Equation 2** retrieves the spectrum, $S(k)$. The minimum number of required interferogram samples, N, is related to the smallest expected fringe spacing caused by the largest expected wavenumber through

$$N \propto 2\frac{k_2}{\delta k}, \qquad [3]$$

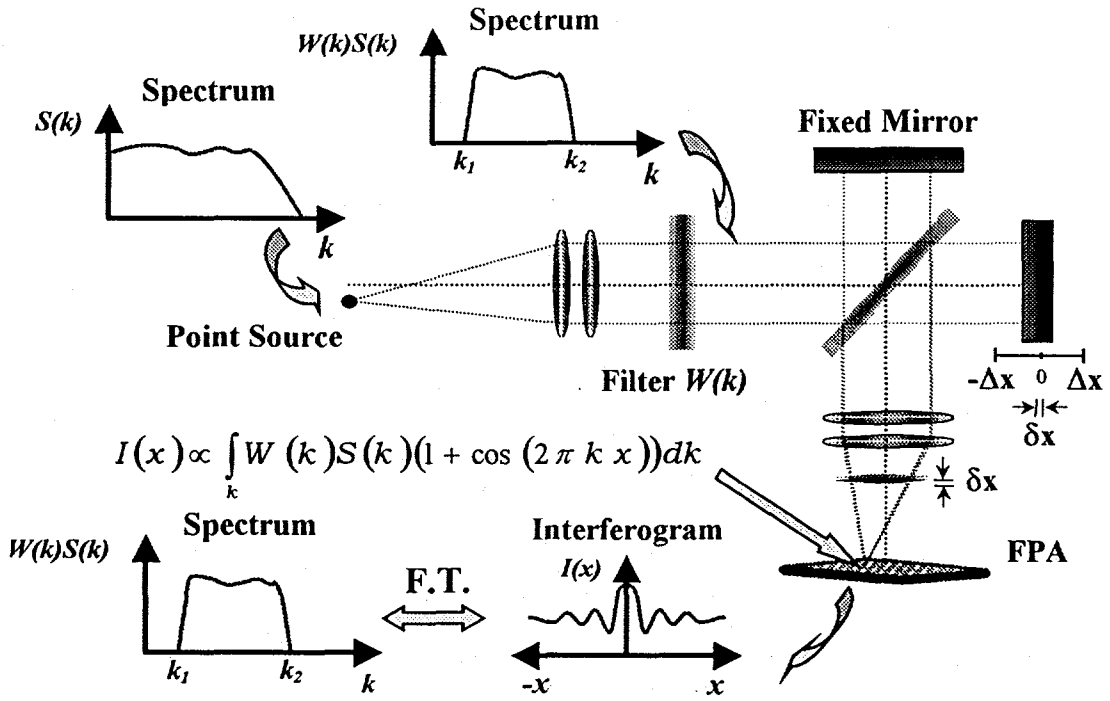

Figure 2. Basic Michelson imaging spectrometer. The interferometer splits the image into two beams, which are recombined at the image plane with relative path difference, δx, introduced by the movable mirror. Sweeping the movable mirror over prescribed travel, $\pm\Delta x$, the interferogram of each imaged point is sequentially sampled at the FPA. Fourier transform of the interferogram retrieves the spectrum.

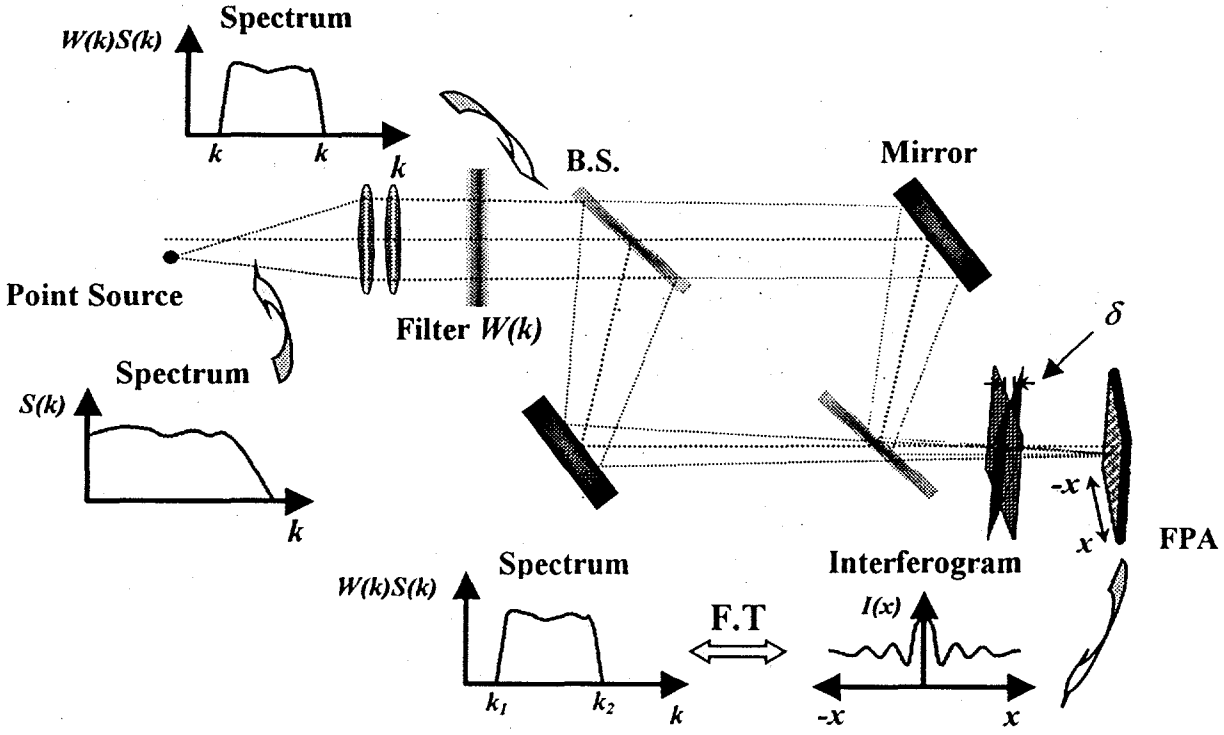

Figure 3. Spatially modulated FTS. The Mach-Zender topology introduces a slight angular tilt in the wavefronts at the image plane. Spatial modulation is accomplished through the linear path difference, δ, introduced by the tilted or crossed wavefronts. Unlike the Michelson imager, the scene must be scanned (pushbroomed) across the image plane for generation of full interferogram.

with the spectral resolution, δk, is determined by the total spatial displacement, $\pm\Delta x$,

$$\delta k \propto \frac{1}{\Delta x}. \qquad [4]$$

Note that as the sample rate specified in **Equation 3** precludes resolving spectral components above k_2, an optical filter, $W(k)$ in **Figure 2**, must band limit the incident spectrum to k_2 or below to prevent spectral retrieval ambiguities resulting from undersampled interferograms.

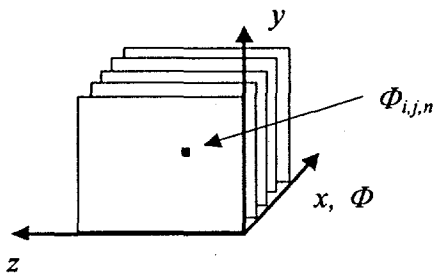

Figure 4. Interferogram data cube with sample element $\Phi_{i,j,n}$. Spatial indices are i, j and the interferogram index is n.

The Michelson imaging spectrometer must dwell in a stationary manner on scene (staring imager) during the interferogram data collection process, that is, over the period of time the mirror is swept, $\pm\Delta x$. An example of the interferogram data cube set is illustrated in **Figure 4**. Each interferogram sample element, $\Phi_{i,j,n}$, corresponds to a one-to-one registration between FPA pixel and scene sample. Retrieval of the scene spectrum at spatial index i,j , $S_{i,j}$, is obtained through Fourier transforming $\Phi_{i,j}$.

An important benchmark of imaging transform spectrometers is the Etendue, ξ, or optical throughput. As the Michelson spectrometer is a staring imager, light is collected over the full field of view and the throughput is maximized. With A_d, the FPA pixel area, and $f_\#$, the effective system F-number, the Michelson throughput is

$$\xi \propto \pi \frac{A_d}{f_\#^2}, \qquad [5]$$

A moving mirror is not the only method of inducing wavefront interference. **Figure 3** schematically illustrates a (highly simplified) spatially modulated spectrometer with no moving parts. Developed by R. F. Horton, the High Etendue Imaging Fourier Transform Spectrometer[6] (HEIFTS) implements a Mach-Zender topology to induce wavefront interference. The optical configuration splits the incoming beam and recombines the wavefronts at the image plane with a slight angular tilt. Spatial modulation is accomplished by way of the linear path difference, δ, introduced by the tilted or "crossed" wavefronts. Unlike the Michelson imaging spectrometer, which operates in the staring mode, HEIFTS is a scanning imager. The scene must be scanned across the image plane to generate the interferogram. When spatially re-indexed to account for scanning, the resulting data cube is similar to that of the Michelson data cube defined in **Figure 4**.

Both the Michelson and HEIFTS effectively share identical optical throughputs and interferogram sampling requirements. However, as the interferogram must be spatially sampled by a given row of FPA pixels, current technological limits may impose practical constraint on the number of pixel samples.

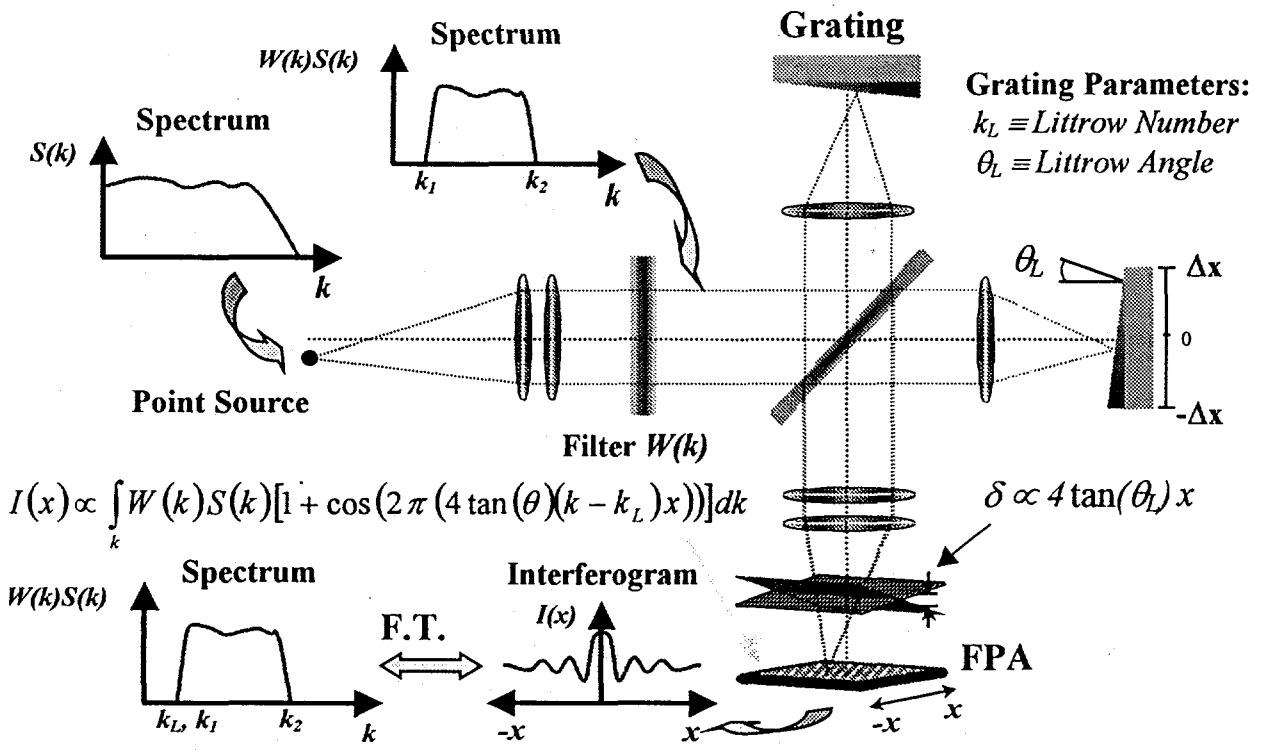

Figure 5. Spatially modulated Imaging SHS. The Imaging SHS utilizes gratings instead of mirrors for the formation of wavefront tilts. The dispersive nature of the gratings leads to a "spatial heterodyne" phenomena whereby the transform cuts off at the Littrow wavenumber, $k = k_L$, instead of the more traditional $k = 0$ permitting a significant savings in required spatial samples. The scene must be scanned (pushbroomed) across the image plane for generation of a full interferogram.

Another approach to spatially modulated FTS, and the objective of this paper, is the infrared Imaging Spatial Heterodyne Spectrometer (ISHS), jointly developed by B. Smith[7, 8] and J. Harlander. Schematically depicted in **Figure 5**, the ISHS is similar in operation to HEIFTS with the exception that gratings instead of mirrors introduce wavefront tilts. Of significance, the dispersive nature of the gratings lead to a "spatial heterodyne" phenomena where the transform cuts off at the Littrow wavenumber, $k = k_L$, instead of the more traditional $k = 0$ wavenumber. As will be shown, this can lead to significant savings in the number of required FPA pixels. The following SHS summary follows from Harlander et al.

The basic spatial heterodyne spectrometer transform is given by

$$\Phi(x) \propto \int_k S(k)[1 + \cos(2\pi(4\tan(\theta_L)(k - k_L)x))]dk \qquad [6]$$

where

$\theta_L \equiv$ Littrow angle,
$k_L \equiv$ Littrow wavenumber [cm^{-1}].

Equation 6 follows from the basic relations governing the generation of Fizeau fringes of wavenumber dependent spatial frequency, which are given by the following grating equation

$$k(\sin(\theta)+\sin(\theta-\gamma))=\frac{m}{d}, \qquad [7]$$

where

$k \equiv$ optical wavenumber [cm^{-1}],
$m \equiv$ order of diffraction,
$\theta \equiv$ Littrow (grating) angle [rad],
$1/d \equiv$ grating groove density [cm^{-1}],
$\gamma \equiv$ angular inclination (relative to optical axis) of crossed wavefronts [rad].

The spatial frequency of the Fizeau fringes of the crossed wavefronts is quantified by

$$f = 2k\sin(\gamma), \qquad [8]$$

and for small γ, is approximated as

$$f \approx 4\tan(\theta)(k-k_L), \qquad [9]$$

with k_L the Littrow ($\gamma = 0$) wavenumber. Substitution of **Equation 9** into the wavefront interference relation given in **Equation 2** results in the SHS equation of **Equation 6**

$$\Phi(x) \propto \int_k S(k)[1+\cos(2\pi(4\tan(\theta_L)(k-k_L)x))]dk.$$

Like the Michelson and HEIFTS, the imaging SHS shares the high optical throughput of **Equation 5**. However the spatial heterodyne phenomena of **Equation 9**, resulting from the dispersive grating, places the transform cut-off at the Littrow wavenumber, $k = k_L$, instead $k = 0$, permitting a reduction in required pixel samples for a given resolution and optical band

$$N \propto 2\frac{k_2-k_L}{\delta k}. \qquad [10]$$

Typically, the Littrow wavenumber, $k = k_L$, is set at or just below the long wave cutoff $k = k_1$.

While the overall fidelity of the captured hyperspectral image is limited and hence determined by both spatial and spectral phenomena, the analysis presented here will focus on SHS spectral error propagation at the detection level. The reader is referred to the literature for performance analysis of the systems spatial response[9,10]. **Sections 2-4** address spectrometer response, retrieval noise, and detection noise. **Section 5** considers calibration issues, while **Section 6** defines basic SHS design relations followed by an SHS design example based on a current experimental laboratory prototype.

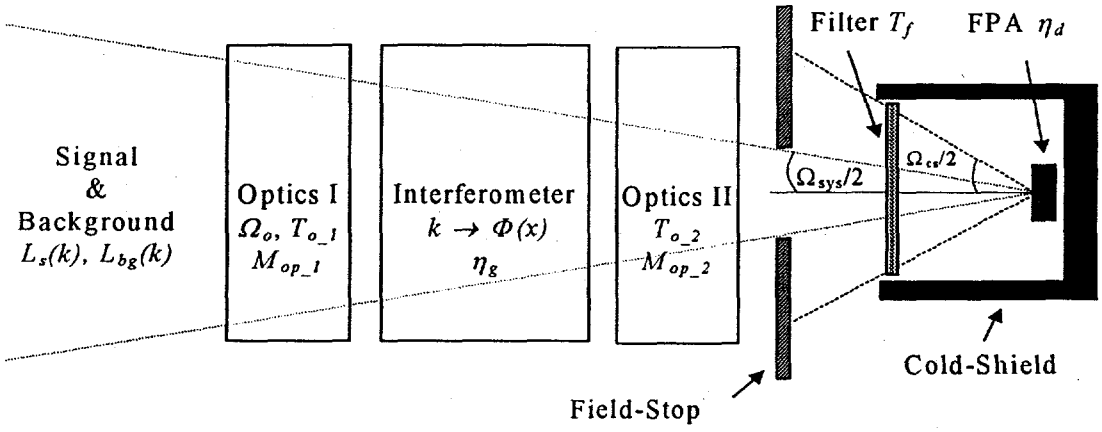

Figure 6. Simplified FTS system depicting composite spectral source approximation and related optical parameters.

2.0 SPECTROMETER RESPONSE

2.1. Detector Referenced Input Spectral Exitance[11]

The FTS's detector referenced input exitance may be approximated by two composite spectral sources: i) radiant sources *imaged* through the spectrometer and contributing, via coherent interference, to the interferogram signal, and ii) *non-imaged* radiant sources that incoherently contribute to the interferogram in the form of DC offset. Referring to **Figure 6**, the detector referenced spectral exitance from all *imaged* radiant sources is given by

$$S_1(k) = \frac{1}{2}\left[\Omega_o\left(L_s(k) + L_{bg}(k)\right) + \frac{\Omega_{sys}}{\pi} M_{op\_1}(k)\right]\chi(k) \qquad [\text{W/m}^2\text{-cm}^{-1}], \qquad [11]$$

while *non-imaged* contributions, typical of radiant sources located after the interferometer, is

$$S_2(k) = \left(\frac{\Omega_{sys}}{\pi}\frac{M_{op\_2}(k)}{T_{o\_1}(k)} + \left(\frac{\Omega_{cs} - \Omega_{sys}}{\pi}\right)\frac{M_{fs}(k)}{T_{o\_1}(k)\eta_g(k)T_{o\_2}(k)} + \left(\frac{\pi - \Omega_{cs}}{\pi}\right)\frac{M_{cs}(k)}{T_{o\_1}(k)\eta_g(k)T_{o\_2}(k)T_f(k)}\right)\chi(k)$$

$$[\text{W/m}^2\text{-cm}^{-1}], \quad [12]$$

where :

$k \equiv$ optical wavenumber [cm^{-1}],
$L_s(k) \equiv$ desired signal radiance [$\text{W/m}^2\text{-sr-cm}^{-1}$],
$L_{bg}(k) \equiv$ undesired (but unavoidable) background radiance [$\text{W/m}^2\text{-sr-cm}^{-1}$],
$M_{op\_1}(k) \equiv$ imaged optical exitance [$\text{W/m}^2\text{-cm}^{-1}$],
$M_{op\_2}(k) \equiv$ non-imaged optical exitance *after* the interferometer [$\text{W/m}^2\text{-cm}^{-1}$],
$M_{fs}(k) \equiv$ field-stop exitance [$\text{W/m}^2\text{-cm}^{-1}$],
$M_{cs}(k) \equiv$ cold-shield exitance [$\text{W/m}^2\text{-cm}^{-1}$];

Aperture and system solid angle [sr]:

$$\Omega_o = \left(1 - \left(\frac{D_{obs}}{D_o}\right)^2\right)\frac{\pi D_o^2}{4 f_1^2}, \qquad [13]$$

$$\Omega_{sys} = \frac{\pi D_o^2}{4 f_1^2}, \qquad [14]$$

$D_o \equiv$ system aperture diameter [m],

$D_{obs} \equiv$ aperture obstruction diameter [m],

$f_1 \equiv$ effective system focal length [m];

Spectral transmission function:

$$\chi(k) = T_{o\_1}(k)\eta_g(k)T_{o\_2}(k)T_f(k)\eta_{d\_n}(k), \qquad [15]$$

$T_{o\_1}(k)$, $T_{o\_2}(k)$ $\equiv$ optical transmission function,

$\eta_g(k) \equiv$ grating efficiency,

$T_f(k) \equiv$ optical filter transmission function,

$\eta_{d\_n}(k) \equiv$ normalized detection quantum efficiency function:

$$\eta_{d\_n}(k) = \frac{\eta_d(k)}{\langle \eta_d \rangle}, \text{ where } \langle \eta_d \rangle \text{ is averaged over the filter passband.} \qquad [16]$$

The optical transmission filter, $T_f(k)$, band-limits the sampled spectrum preventing or reducing spectral aliasing. The signal and background spectral radiance's, $L_s(k)$ and $L_{bg}(k)$, should be generated with high spectral resolution, i.e. HITRAN or MODTRAN depending on required spectral resolution.

2.2. Interferogram Generation and Inversion[12]

Substitution of sources $S_1(k)$ and $S_2(k)$ into **Equation 6** results in the following image-plane referenced interferogram

$$\Phi(x) = \Im\left\{\frac{1}{hc}\int_k \frac{S_1(k)}{k}\left[1 + \cos\left(2\pi\left(4\tan(\theta_L)(k - k_L)x\right) + \theta(k,x)\right)\right]dk\right\} + \frac{1}{hc}\int_k \frac{S_2(k)}{k}dk \qquad [17]$$

[ph/m^2-s],

where:

$h \equiv$ Plank's constant [6.626 10^{-34} J-s],

$c \equiv$ speed of light [2.998 10^{8} m/s],

$\Im(k,x)$: A functional dependency accounting for coherent detection effects including fringe visibility "washout", distortion, and spatial sampling.

$\theta(k,x)$: A functional additive phase dependency accounting for wave dispersion and systematic phase distortion.

In many cases, the functional dependency, $\Im$, is a multiplicative function, and the interferogram of **Equation 17** can be re-written as the sum of an offset plus interferogram:

$$\Phi(x) = \Phi_o + \frac{1}{hc}\int_k \frac{S_1(k)}{k}\Im(k,x)\cos(2\pi(4\tan(\theta_L)(k-k_L)x) + \theta(k,x))dk \quad [\text{ph/m}^2\text{-s}], \quad \textbf{[18]}$$

with the offset

$$\Phi_o = \frac{1}{hc}\int_k \frac{1}{k}(S_1(k) + S_2(k))dk \qquad [\text{ph/m}^2\text{-s}]. \qquad \textbf{[19]}$$

Retrieval of the image spectrum $L_s(k)$ and $L_{bg}(k)$ follows from inversion of **Equations 11** and **18**

$$L_s(k) + L_{bg}(k) = \frac{1}{\Omega_o}\left(\frac{S_1(k)}{\chi(k)} - \frac{\Omega_{sys}}{\pi}M_{op\_1}(k)\right) \qquad [\text{W/m}^2\text{-sr-cm}^{-1}], \qquad \textbf{[20]}$$

and

$$S_1(k) = hc\,K\,4\tan(\theta_L)\int_k k(\Phi(x) - \Phi_o)\Im^{-1}(k,x)\cos(2\pi(4\tan(\theta_L)(k-k_L)x) + \theta(k,x))dx$$

$$[\text{W/m}^2\text{-cm}^{-1}], \quad \textbf{[21]}$$

where K = 4 or 2 for a single or double sided transform respectively , and it has been assumed that the inverse, $\Im^{-1}$, exists.

2.3. Sampled SHS[13,14]

As an image plane FPA will spatially sample the interferogram, **Equations 18 - 21** will have to be discretized. For $n = 0,1,2,3 .. N-1$ samples, **Equations 18 - 21** result in:

$$\Phi_n = \Phi_o + \frac{1}{hc}\sum_{m=0}^{N-1}\frac{S_{1m}}{k_m}\Im(k_m,x_n)\cos(2\pi(4\tan(\theta_L)(k_m-k_L)x_n) + \theta(k_m,x_n))\delta k$$

$$[\text{ph/m}^2\text{-s}], \qquad \textbf{[22]}$$

$$\Phi_o = \frac{1}{hc}\sum_{m=0}^{N-1}\frac{1}{k_m}\left(S_{1m} + S_{2m}\right)\delta k \qquad [\text{ph/m}^2\text{-s}], \tag{23}$$

$$L_{s_n} + L_{bg_n} = \frac{1}{\Omega_o}\left(\frac{S_{1n}}{\chi_n} - \frac{\Omega_{sys}}{\pi}M_{op\_1n}\right) \qquad [\text{W/m}^2\text{-sr-cm}^{-1}], \tag{24}$$

$$S_{1_n} = hc\,\mathrm{K}\,4\tan(\theta_L)\sum_{m=0}^{N-1}k_n\left(\Phi_m - \Phi_o\right)\Im^{-1}(k_n, x_m)\cos\left(2\pi\left(4\tan(\theta_L)(k_n - k_L)x_m\right) + \theta(k_n, x_m)\right)\delta x$$

$$[\text{W/m}^2\text{-cm}^{-1}], \tag{25}$$

where:

$$k_n = k_L + n\delta k \quad n = 0,1,2,3\ldots N-1, \quad \text{with } k_L \equiv \text{Littrow wavenumber } [\text{cm}^{-1}], \tag{26}$$

$$x_n = n\delta x - x_o \quad n = 0,1,2,3\ldots N-1, \tag{27}$$

$$k_{nyq} = k_L + \delta k\frac{N}{2} \text{ (Nyquist wavenumber)}, \tag{28}$$

and x_o a spatial offset depending on single or double sided interferometer configurations.

To reconstruct the spectral wavenumber k_{nyq}, Whittaker-Shannon sampling theorem requires a sample rate of at least $2k_{nyq}$. The sample rate of $2k_{nyq}$ is known as the Nyquist rate and the k_{nyq} the Nyquist wavenumber. Any wavenumbers below k_{nyq} will be unambiguously reconstructed while wavenumbers above k_{nyq} are aliased. To prevent spectral aliasing, T_f (or χ) must sufficiently attenuate spectral components at and beyond k_{nyq}.

A) Coherent Detection

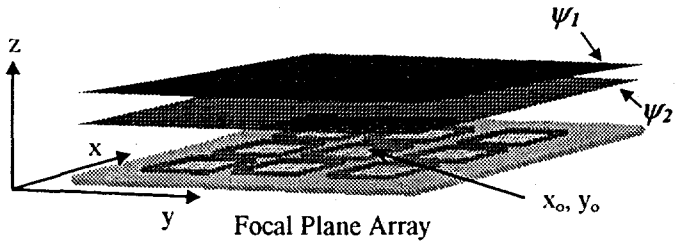

- Spatial Coherence Function

$$\rho(k,x) = \rho_o(k)e^{-\left|\frac{x}{\rho_c(k)}\right|^{\rho_e(k)}}$$

$\rho_c \equiv$ Coherence Length [m]
$\rho_e \equiv$ Exponential Coefficient []

B) Interferogram - Intensity Distribution

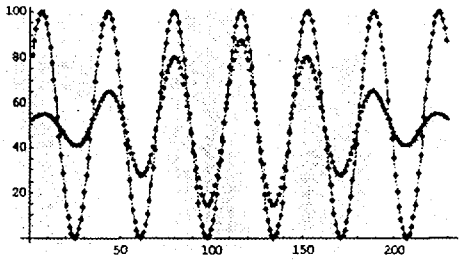

C) Interferogram - Fringe Pattern

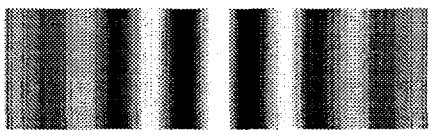

Figure 7. A) Example of spatial coherence demonstrating fringe visibility loss or "washout" due to coherence degradation for function parameters $\rho_o = 3/4$, $\rho_c = 1/3\ X_{array}$, $\rho_e = 2$. **B)** SHS interferogram intensity distribution and **C)** fringe pattern. As fringe contrast is prematurely lost into the background, detection noise will increase.

2.4. Spatial Coherence

Degradations in spatial coherence can lead to interferogram fringe distortion and reduction in fringe visibility resulting in retrieval error and increases in detection noise. The derivation of the FTS coherent detection process follows from Poynting's relation[15,16,17] which relates the induced detector current, I, to the detector's quantum efficiency, $\eta(x,y)$, and the spatial distribution of the interfering electromagnetic fields, ψ_1 and ψ_2, respectively, over the FPA detection surface, s, as depicted in **Figure 7** through

$$I = k_c \iint_s \eta(\mathbf{E}\times\mathbf{H})\cdot d\mathbf{s}, \quad k_c \equiv constant, \quad [\mathrm{A}]. \qquad \textbf{[29]}$$

Assuming the fields are transverse electromagnetic in nature, and of the form

$$\mathbf{E} \equiv \psi_1(x,y)e^{i\omega t + iz_1(x,y)k} + \psi_2(x,y)e^{i\omega t + iz_2(x,y)k}, \quad \mathbf{H} \equiv \sqrt{\frac{\varepsilon}{\mu}}\mathbf{E}, \qquad \textbf{[30]}$$

results in the induced pixel current

$$I = k_c \sqrt{\frac{\varepsilon}{\mu}}\,\mathrm{Re}\left[\iint_{A_d} \eta(x,y)\left|\psi_1(x,y)e^{iz_1(x,y)k} + \psi_2(x,y)e^{iz_2(x,y)k}\right|^2 dx\,dy\right]. \qquad \textbf{[31]}$$

The resulting pixel current, a superposition of the non-interfering plus a interfering wavefront terms, is a result of field amplitude and path difference (phase) distributions, $|z_1(x,y) - z_2(x,y)|$, integrated over the pixel surface. As will be demonstrated in the following derivation, irregularities in the microscopic and macroscopic field distributions can lead to fringe distortion and loss of fringe visibility.

Equation 31 reduces to **Equation 1** by sampling the fields at the pixel centers through the substitution $\eta(x,y) \rightarrow \eta_o \cdot \delta(x-x_o) \cdot \delta(y-y_o)$, resulting in the familiar relation

$$\Phi_o \propto \psi_{1_o}^2 + \psi_{2_o}^2 + 2\psi_{1_o}\psi_{2_o}\cos(2\pi(z_1 - z_2)k).$$

Furthermore, substitution of the SHS relation, $z_1 - z_2 = 4\tan(\theta_L)(k-k_L)x$, normalizing the fields, and integration over spectrum, $S(k)$, leads to the SHS relation

$$\Phi(x) \propto \int_k \frac{S(k)}{k}\left[1 + \cos(2\pi(4\tan(\theta_L)(k-k_L)x))\,dk\right].$$

The spatial coherence degradation of **Equation 31** may be approximated by spatially integrating over the finite pixel pitch, Δ_x, and the inclusion of the spatial coherence function $\rho(k,x)$

$$\Phi(x) \rightarrow \int_k \frac{S(k)}{k}\left[1 + \rho(k,x)\,\mathrm{sinc}(4\tan(\theta_L)(k-k_L)\Delta_x)\cos(2\pi(4\tan(\theta_L)(k-k_L)x))\right]dk. \qquad \textbf{[32]}$$

The spatial coherence function, $\rho(k,x)$, may be represented as the product of self and cross coherence term, $\rho(k,x) = \rho_o(k)\rho_x(k,x)$. The self-coherence term models the microscopic intra-pixel coherence degradation (reduction in fringe intensity at zero-path difference) due to small-scale quantum efficiency variations and optical field distortion over the detector surface. The macroscopic cross-coherence term accounts for inter-pixel coherence degradation (reduction in fringe visibility across the image plane) via large-scale field distortion including optical system aberrations, alignment etc. While coherence effects are typically complex, a simple analytic model illustrating fringe visibility loss is given by

$$\rho(k,x) = \rho_o(k)e^{-\left|\frac{x}{\rho_c(k)}\right|^{\rho_e(k)}}. \qquad [33]$$

The model is based on Gaussian phase screens[18] with ρ_o is the self coherence term, ρ_c is the spatial coherence length, and ρ_e exponent. **Figure 7** demonstrates fringe visibility loss or "washout" due to coherence degradation for $\rho_o = 3/4$, $\rho_c = 1/3\ \Delta x_{array}$, $\rho_e = 2$. As fringe contrast is prematurely lost into the background, detection noise increases. Throughout the remainder of the paper, the placeholder function, $\Im(k,x)$, defined in **Equations 22, 25** will assume the value

$$\Im(k,x) \equiv \rho(k,x)\mathrm{sinc}(4\tan(\theta_L)(k-k_L)\Delta_x). \qquad [34]$$

3.0 DETECTION NOISE

3.1. Stationary Noise Process[19,20,21]

Analysis of noise propagation in the FTS spectrum begins with the examination of noise induced variations of the intensity interferogram. From **Equations 22** and **23**, we define the interferogram fluctuations or *fringe contrast* as

$$\Phi_{\sigma_n} \equiv \Phi_n - \Phi_\mu \quad [\mathrm{ph/m^2\text{-}s}], \qquad [35]$$

with the interferogram *offset* or mean as

$$\Phi_\mu \equiv E[\Phi_n] \quad [\mathrm{ph/m^2\text{-}s}]. \qquad [36]$$

Note that for stationary noise, the interferogram mean converges to Φ_o for n large

$$\Phi_\mu \equiv \langle \Phi_n \rangle \to \Phi_o \quad [\mathrm{ph/m^2\text{-}s}]. \qquad [37]$$

The detection signal to noise ratio referenced at the detector (SNR_x) will be estimated in this paper by evaluating the *fringe contrast* to noise ratio

$$SNR_{x_n} = \frac{|\Phi_{\sigma_n}|}{\sigma_{x_n}}, \qquad [38]$$

where, in terms of root-mean-square (rms) noise equivalent radiance,

$$\sigma_{x_n} = NEI_{tot_n} = \sqrt{NEI_{ph_n}^2 + NEI_{dar}^2} \quad [\text{ph/m}^2\text{-s}], \tag{39}$$

and

$$NEI_{ph_n} = \sqrt{\kappa_d \frac{\Delta f}{\langle \eta_d \rangle A_d} \Phi_n} \quad [\text{ph/m}^2\text{-s}], \tag{40}$$

$\kappa_d \equiv$ detection noise factor,

$A_d \equiv$ detector element (pixel) area [m^2],

$\Delta f \equiv$ noise equivalent bandwidth [Hz],

$NEI_{dar} \equiv$ equivalent detector, amplifier and readout noise [ph/m^2-s].

The NEI_{dar} of **Equation 39** is the total detector, amplifier and readout noise, and is related to the detector/amplifier/readout noise spectral density, n_{dar} (defined in volts or amps per $\sqrt{\text{Hz}}$), through

$$NEI_{dar} = \sqrt{k_{dar}^2 \int_f |n_{dar}(f)|^2 df} \quad [\text{ph/m}^2\text{-s}], \tag{41}$$

where k_{dar} is a conversion constant (V or A to NEI) and f [Hz] the frequency variable. **Equation 41** is valid for both white and colored (correlated) noise types.

Finally, the spectral signal to noise ratio, assuming Gaussian noise, of the retrieved spectrum, SNR_k, for the n^{th} spectral component will be defined as

$$SNR_{k_n} \equiv \frac{S_{1_n}}{\sigma_{k_n}}, \tag{42}$$

with σ_k estimated through (see **Appendix A**)

$$\sigma_{k_n} = hc\,\mathrm{K}\,4\tan(\theta_L)\sqrt{\delta x \sum_{m=0}^{N-1} \left| k_n \Im^{-1}(k_n, x_m) k_n \cos\left(2\pi\left(4\tan(\theta_L)(k_n - k_L)x_m\right) + \theta(k_n, x_m)\right)\right|^2 \sigma_{x_m}^2 \delta x} \quad [\text{W/m}^2\text{-cm}^{-1}]. \tag{43}$$

Equation 43 demonstrates the n^{th} spectral noise component is composed of the summed contributions from all the interferogram noise terms, σ_x, modulated by the magnitude squared of the inversion relation given in **Equation 25**.

3.1. Non-Stationary Noise Processes[22,23]

In the presence of non-stationary noise (varying mean and covariance), the estimation process defined by **Equation 35** is invalid because the interferogram mean becomes non-stationary

$$\Phi_\mu(n) \equiv E\left[\Phi_n(n)\right] \neq \Phi_o \quad \text{[ph/m}^2\text{-s]}. \qquad \textbf{[44]}$$

The inversion relation, which is now expressed in terms of a mean that varies as a function of sample index, *m*, results in a corrupted spectral retrieval, S_I

$$S_{I_n} = hc\,\mathrm{K}\,4\tan(\theta_L)\sum_{m=0}^{N-1} k_n\left(\Phi_m - \Phi_\mu(m)\right)\Im^{-1}(k_n, x_m)\cos(2\pi(4\tan(\theta_L)(k_n - k_L)x_m) + \theta(k_n, x_m))\delta x$$

$$\text{[W/m}^2\text{-cm}^{-1}\text{]}. \qquad \textbf{[45]}$$

The most common causes of a non-stationary mean are low-frequency drifts in the spatial and/or temporal sampling process, i.e. a spatial row of channels or a single-channel time sampled sequence. Higher frequency sources would include, for example, jitter and vibrations due to platform motion.

A comparative summary of the three most typical noise types include:

- White Noise: The 'ideal' noise process with constant mean and covariance.

$$\Phi_\mu \to \Phi_o \quad \text{[ph/m}^2\text{-s]}. \qquad \textbf{[46]}$$

- Systematic + White Noise: A systematic linear trend in the interferogram mean with a slope of $\pm\varepsilon$, over the temporal/spatial sample space $n = 0, 1, 2, 3, \ldots N-1$

$$\Phi_\mu(n) \to \Phi_o \pm \varepsilon n \quad \text{[ph/m}^2\text{-s]}. \qquad \textbf{[47]}$$

  Typical sources of systematic noise include i) a slow temperature drift in the near field blackbody or focal plane array (i.e. optics, filter, cold shield, detector dark current etc.), ii) electronic detector, amplifier and readout offset drift, and iii) amplifier gain drift. Systematic noise may be removed, to first order, by a two-point calibration where the system is calibrated immediately before and after a measurement sequence (see **5.0 Calibration**).

- Correlated 1/f + White Noise: Noise sources introducing significant levels of correlated, low frequency noise (effectively a nonlinear drift over the acquisition window) resulting in a poor interferogram mean estimate and the probable corruption of the retrieved spectrum, S_I. Calibration is extremely difficult as the mean is a nonlinear function of sample *n*

$$\Phi_\mu(n) \to E\left[\Phi_n(n)\right] \neq \Phi_o \quad \text{[ph/m}^2\text{-s]}. \qquad \textbf{[48]}$$

4.0 INTEGRATING PHOTOVOLTAIC CELL

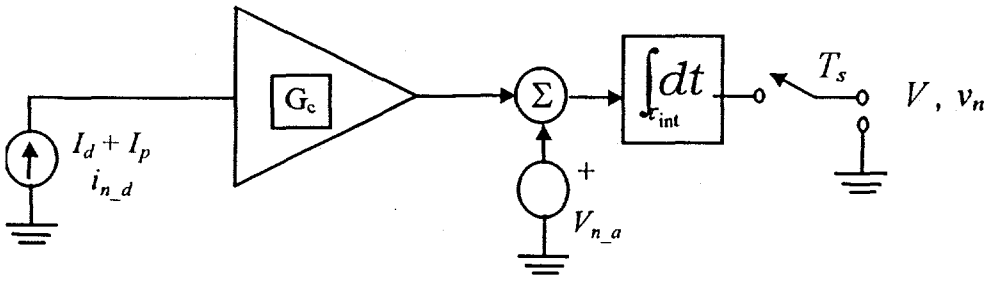

Figure 8. Basic integrating photovoltaic FPA cell block diagram.

The simplified block diagram of a basic, integrating photovoltaic, focal plane array cell[24,25,26] (IPV FPA) is shown in **Figure 8**. IPV FPA's are the most common form of infrared focal plane array topologies, encompassing categories from the simple direct injection (DI) cell to the more complex capacitive transimpedance amplifier (CTIA). Basically, the IPV stores injected detector current as charge on a capacitive integrating node for later readout at a sample period T_s. The cell's output is a voltage value determined by the stored charge, node capacitance, and any additional cell gain. Referring to **Figure 8**, the IPV output signal and noise voltage relations are evaluated as

$$V = G_c\, \tau_{\text{int}} \left(I_d + I_p \right) \quad \text{[V]}, \tag{49}$$

$$v_n = \sqrt{\left(i_{n\_d}^2 \left| G_c\, \tau_{\text{int}} \right|^2 + v_{n\_a}^2 \right) \Delta f} \quad \text{[V]}, \tag{50}$$

where:

$T_s \equiv$ sample period (frame rate) [s],
$\tau_{int} \equiv$ integration period (Note: $\tau_{int} \leq T_s$) [s],
$G_c \equiv$ amplifier conversion gain [V/q],
$A_d \equiv$ detector element (pixel) area [m^2],
$\Delta f \equiv 1/2T_s$ noise equivalent bandwidth [Hz],
$I_d \equiv$ detector dark current [A],
$I_p \equiv q\, A_d\, \eta_d\, \Phi$ detector photocurrent [A],
$\eta_d \equiv$ detection quantum efficiency,
$\kappa_d \equiv$ detection noise factor ($\kappa_d = 2$ for photovoltaic),
$v_{n\_a} \equiv$ amplifier/read output referred noise voltage [V/$\sqrt{}$Hz],
$i_{n\_d} \equiv$ detection noise current:

$$i_{n\_d} = \sqrt{q \kappa_d \left(I_d + I_p \right)} \quad \text{[A/}\sqrt{}\text{Hz]}. \tag{51}$$

Substitution of the relevant relations derived in **Sections 2** and **3** into **Equations 49 - 51** result in the following sampled voltage expressions ($n = 0,1,2,3, \ldots N\text{-}1$):

$$V_n = G_c\,\tau_{\text{int}}\left(I_d + q\,A_d\,\langle\eta_d\rangle\,\Phi_n\right) \quad \text{[V]}, \tag{52}$$

$$V_\mu(n) = E\left[V_n(n)\right] \quad \text{[V]}, \tag{53}$$

$$V_{\sigma_n} = V_n - V_\mu(n) \quad \text{[V]}, \tag{54}$$

$$S_{1_n} = \frac{hc\,\mathrm{K}\,4\tan(\theta_L)}{q\,G_c\,\tau_{\text{int}}\,A_d\langle\eta_d\rangle}\sum_{m=0}^{N-1} k_n\,V_{\sigma_m}\,\Im^{-1}(k_n,x_m)\cos\left(2\pi\left(4\tan(\theta_L)(k_n-k_L)x_m\right)+\theta(k_n,x_m)\right)\delta x$$

$$\text{[W/m}^2\text{-cm}^{-1}\text{]}, \tag{55}$$

$$\sigma_{x_n} = v_{n_n} = \sqrt{\left(q\,\kappa_d\left(I_d + q\,A_d\,\langle\eta_d\rangle\,\Phi_n\right)\left|G_c\,\tau_{\text{int}}\right|^2 + v_{n\_a}^2\right)\Delta f} \quad \text{[V]}, \tag{56}$$

$$\sigma_{k_n} = \frac{hc\,\mathrm{K}\,4\tan(\theta_L)}{q\,G_c\tau_{\text{int}}\,A_d\langle\eta_d\rangle}\sqrt{\delta x\sum_{m=0}^{N-1}\left|k_n\Im^{-1}(k_n,x_m)k_n\cos\left(2\pi\left(4\tan(\theta_L)(k_n-k_L)x_m\right)+\theta(k_n,x_m)\right)\right|^2\sigma_{x_m}^2\,\delta x}$$

$$\text{[W/m}^2\text{-cm}^{-1}\text{]}, \tag{57}$$

and signal to noise,

$$SNR_{x_n} = \frac{\left|V_{\sigma_n}\right|}{\sigma_{x_n}}, \qquad SNR_{k_n} = \frac{S_{1n}}{\sigma_{k_n}}. \tag{58}$$

5.0 CALIBRATION

The detection noise and resulting spectral retrieval fidelity are closely linked to the calibration methodology. A brief summary of calibration in the presence of noise using the detection noise framework defined in **Section 2.0 – 4.0** follows.

5.1. Calibration Source

Ideally, a set of known calibration sources, $l = 1,2,\ldots l_{max}$, of uniform temperature and emissivity, are sequentially inserted at the FTS input generating a set of $l = 1,2,\ldots l_{max}$ linearly independent input/output relations with which to characterize or calibrate up to l_{max} system unknowns. For a set of calibration sources, $l = 1,2,\ldots l_{max}$, the detector referenced input spectral exitance, **Equation 11**, is modified with

$$S_{1_{l,n}} \rightarrow S_{cal_{l,n}}(\varepsilon_l, T_l) = \frac{1}{2}\left[\frac{\Omega_o}{\pi}M_{cal_n}(\varepsilon_l, T_l) + \frac{\Omega_{sys}}{\pi}M_{op\_1_n}\right]\chi_n \quad \text{[W/m}^2\text{-cm}^{-1}\text{]}, \tag{59}$$

where:

$l = 1,2,\ldots l_{max}$ ≡ the number of calibrated sources,
T_l ≡ temperature of the l^{th} source [T],
ε_l ≡ emissivity of the l^{th} source.

5.2. Minimum Source Set: Ideal Spectral Calibration

It follows from **Equation 59** that the input/output relations of an idealized FTS calibration, given $l = 1,2,\ldots l_{max}$ calibration sources, can be written as

$$S_{m_{l,n}} = S_o \delta(n) + \frac{\Omega_o}{\pi} M_{cal_n}(\varepsilon_l, T_l)\chi_n + \frac{\Omega_{sys}}{\pi} M_{op\_1_n}\chi_n \quad [\mathrm{W/m^2\text{-}cm^{-1}}], \qquad \textbf{[60]}$$

with the known and unknown terms:

knowns:

S_m ≡ spectrometer output - total measured optical exitance [$\mathrm{W/m^2\text{-}cm^{-1}}$],
M_{cal} ≡ optical exitance of the l^{th} calibration source [$\mathrm{W/m^2\text{-}cm^{-1}}$],
Ω_o, Ω_{sys} ≡ aperture and system solid angle [sr]:

unknowns:

$S_o\ \delta(n)$ ≡ optical exitance at $n=0$ due to radiation from source S_2 and channel offset (Note: $\delta(n)$ ≡ kronecker delta function) [$\mathrm{W/m^2\text{-}cm^{-1}}$],
M_{op_1} ≡ *imaged* optical exitance entering the interferometer [$\mathrm{W/m^2\text{-}cm^{-1}}$],
$\chi_n \equiv T_{o\_1_n}\,\eta_{g_n}\,T_{o\_2_n}\,T_{f_n}\,\eta_{d\_n_n}$ spectral transmission function.

Given the three unknowns, a minimum number of three calibrated sources are required, resulting in the following set of input/output relations

$$\begin{aligned}
S_{m_{1,n}} &= S_o\,\delta(n) + \frac{\Omega_o}{\pi} M_{cal_n}(\varepsilon_1, T_1)\,\chi_n + \frac{\Omega_{sys}}{\pi} M_{op_1_n}\,\chi_n \\
S_{m_{2,n}} &= S_o\,\delta(n) + \frac{\Omega_o}{\pi} M_{cal_n}(\varepsilon_2, T_2)\,\chi_n + \frac{\Omega_{sys}}{\pi} M_{op_1_n}\,\chi_n \\
S_{m_{3,n}} &= S_o\,\delta(n) + \frac{\Omega_o}{\pi} M_{cal_n}(\varepsilon_3, T_3)\,\chi_n + \frac{\Omega_{sys}}{\pi} M_{op_1_n}\,\chi_n
\end{aligned} \qquad \textbf{[61]}$$

from which S_o, M_{op_1}, and χ are to be estimated. As will be demonstrated next, the offset component S_o can be estimated directly from the interferogram, reducing the number of required calibrated sources by one.

5.3. Estimating FTS Channel Gain and Offset

Each FTS channel, for a modern focal-plane array (FPA), consists of a detector "looking" into a radiant background, an amplifier and a readout (the A/D conversion will be considered common to all channels). In general, each channel differs slightly in gain and offset due to minute channel-to-channel variations in detector, amplifier, readout and observed radiant background. Furthermore, the variations can be static or spatial/temporal functions. The spatial/temporal dependence can be deterministic or random in nature, and if random, both stationary and non-stationary processes can be present. The output voltage of the p,q channel of a PxQ FTS array is given by **Equation 52**,

$$V_{p,q,n} = G_{c_{p,q}} \tau_{\text{int}_{p,q}} \left(I_{d_{p,q}} + q A_{d_{p,q}} \left\langle \eta_{d_{p,q}} \right\rangle \Phi_{p,q,n} \right) \quad \text{[V]}, \tag{62}$$

The gain of the p,q channel reduces to the term

$$Gain_{p,q} = q G_{c_{p,q}} \tau_{\text{int}_{p,q}} A_{d_{p,q}} \left\langle \eta_{d_{p,q}} \right\rangle \quad \text{[V/(ph/m}^2\text{-s)]}, \tag{63}$$

and the offset voltage (for a stationary noise process)

$$V_{\mu_{p,q}} = G_{c_{p,q}} \tau_{\text{int}_{p,q}} \left(I_{d_{p,q}} + q A_{d_{p,q}} \left\langle \eta_{d_{p,q}} \right\rangle \Phi_{o_{p,q}} \right) \quad \text{[V]}. \tag{64}$$

With the offset estimated, the zero-mean voltage interferogram will be defined with

$$V_{\sigma_{p,q,n}} = V_{p,q,n} - V_{\mu_{p,q}} \quad \text{[V]}. \tag{65}$$

From **Equation 55**, the total measured exitance, S_m, is evaluated and the calibration input/output relations of **Equation 61** reduce to the following:

$$\begin{aligned} S_{m_{1,p,q,n}} &= \frac{\Omega_o}{\pi} M_{cal_{p,q,n}}(\varepsilon_1, T_1) \chi_{p,q,n} + \frac{\Omega_{sys}}{\pi} M_{op\_1_{p,q,n}} \chi_{p,q,n} \\ S_{m_{2,p,q,n}} &= \frac{\Omega_o}{\pi} M_{cal_{p,q,n}}(\varepsilon_2, T_2) \chi_{p,q,n} + \frac{\Omega_{sys}}{\pi} M_{op\_1_{p,q,n}} \chi_{p,q,n} \end{aligned}, \tag{66}$$

with M_{op_1} and χ the remaining unknowns. Note that in general, the channel gain may be a nonlinear function of irradiance, Φ,

$$Gain_{p,q} \rightarrow Gain_{p,q}(\Phi) \quad \text{[V/(ph/m}^2\text{-s)]}, \tag{67}$$

and for the non-stationary noise of **Section 3.1.**, **Equation 63** becomes sample dependent

$$V_{\mu_{p,q}} \rightarrow V_{\mu_{p,q}}(n) = E\left[V_{n,p,q}(n) \right] \quad \text{[V]}. \tag{68}$$

In summary, for every channel p,q, a given calibration algorithm will be required to estimate the gain/offset evaluating M_{op_1} and χ as prescribed by **Equations 63** through **66**. A minimum of two calibrated sources is suggested for channels linear in gain and offset, while three or more sources may be required to calibrate channels with increasing degrees of nonlinearity.

6.0 BASIC SHS DESIGN

6.1. Spatial Interferometer Parameters

The fundamental SHS spatial interferometer equations, based on combined spectrometer and dispersive grating relations, results in a set of nonlinear design relations that must be simultaneously iterated for a self-consistent generation of interferometer design parameters. This section summarizes basic design relations permitting the iteration and generation of first order spatial interferometer design parameters and constraints. The first order design parameters essentially provide a starting point for the SHS design through the system performance analysis discussed in **Sections 2.0 – 5.0** and optical design.

Spatial interferometer parameters:

$k_1 - k_2 \equiv$ spectral range [cm^{-1}],
$\delta k \equiv$ spectral resolution [cm^{-1}],
$N \equiv$ number of interferogram samples (pixels),
$\delta x \equiv$ sample pitch, $\delta x \leq$ pixel pitch Δ_x [cm],
$W \equiv$ grating width [cm],
$d_g \equiv$ grating groove density [grooves/cm],
$\theta_L \equiv$ Littrow angle [rad],
$k_L \equiv$ Littrow wavenumber [cm^{-1}]

Referring to **Figure 5** and the FTS and SHS equations defined in **Equations 6-10**, the design parameters may be iterated through the following spatial interferometer design relations.

SHS spatial Interferometer design relations:

1. Maximum grating path difference:

$$X_{\max} = \frac{1}{2} W \cos(\theta_L) \qquad \text{[cm]} \qquad \textbf{[69]}$$

2. Spectral resolution:

$$\delta_k = \frac{1}{2(4 \tan(\theta_L) X_{\max})} \qquad [\text{cm}^{-1}] \qquad \textbf{[70]}$$

3. Littrow wavenumber (*require* $k_L \leq k_1$):

$$k_L = \frac{d_g}{2\sin(\theta_L)} \quad [\text{cm}^{-1}] \qquad [71]$$

4. Number of samples (*round up to nearest integer*):

$$N = 2\left[4W(k_2 - k_L)\sin(\theta_L)\right] \qquad [72]$$

5. Nyquist sample pitch (*require* $\delta x \leq$ *pixel-pitch* Δ_x):

$$\delta x = \frac{1}{4\tan(\theta_L)\delta k N} \quad [\text{cm}] \qquad [73]$$

6. Nyquist wavenumber (*require* $k_{nyq} \geq k_2$):

$$k_{nyq} = k_L + \delta k \frac{N}{2} \quad [\text{cm}^{-1}] \qquad [74]$$

6.2. SHS System Analysis

Once the basic spatial interferometer design parameters have been identified, the system analysis tools defined in **Sections 2.0 – 5.0** may be used to further specify and optimize additional system parameters and design. Additional system parameters include aperture dimensions, f-number, spectral transmission, cold-shield, optical filtering and focal-plane responsivity and readouts, calibration issues, and data processing including retrieval algorithms.

6.3. Design Example

An SHS design example based on a current experimental laboratory prototype follows. The desired target performance requirements are a spectral bandwidth of k_1 = 1053 cm^{-1} to k_2 = 1176 cm^{-1} at a resolution of δk = 1 – 2 cm^{-1}. Furthermore, as the experiment will utilize a commercially available grating and FPA, the design is constrained to a groove density of 500 cm^{-1} and a 256x256 by 30 μm pitch array. The iterated interferometer and remaining system parameters are summarized below.

Interferometer parameters:

k_1 , k_2 = 1053 cm^{-1} - 1176 cm^{-1}
N = 256,
W = 1.05 cm,
θ_L = 13.75 Deg.,
δk =1.33 cm^{-1},
δx = 30 μm,
d_g = 500 cm^{-1},
k_L = 1052 cm^{-1},
k_{nyq} = 1222 cm^{-1}.

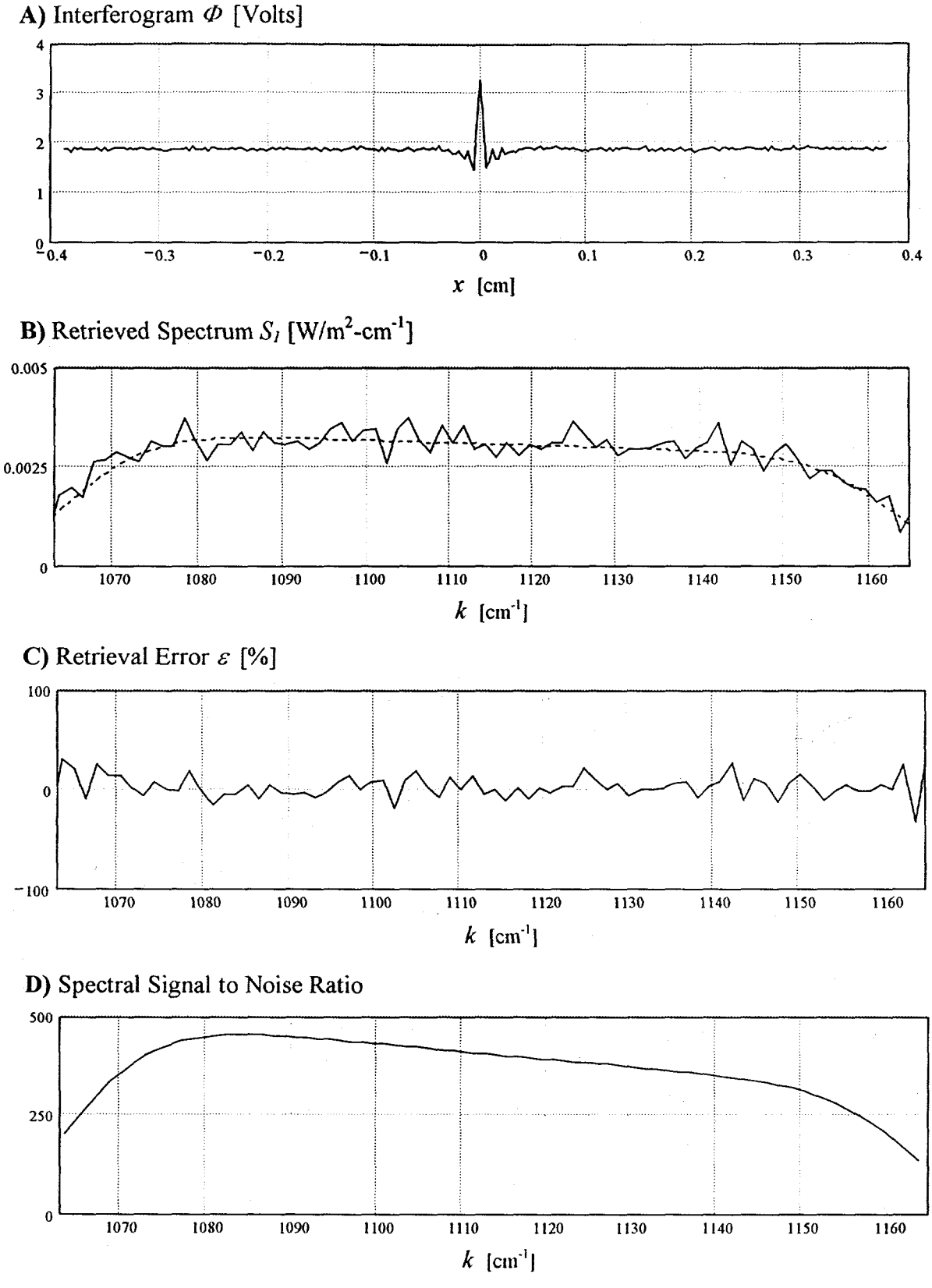

Figure 9. Uncalibrated response: **A)** Interferogram Φ, **B)** Retrieved spectrum S_I, **C)** Relative retrieval error, and **D)** Spectral signal to noise ratio. A 1% gain and offset non-uniformity was assumed.

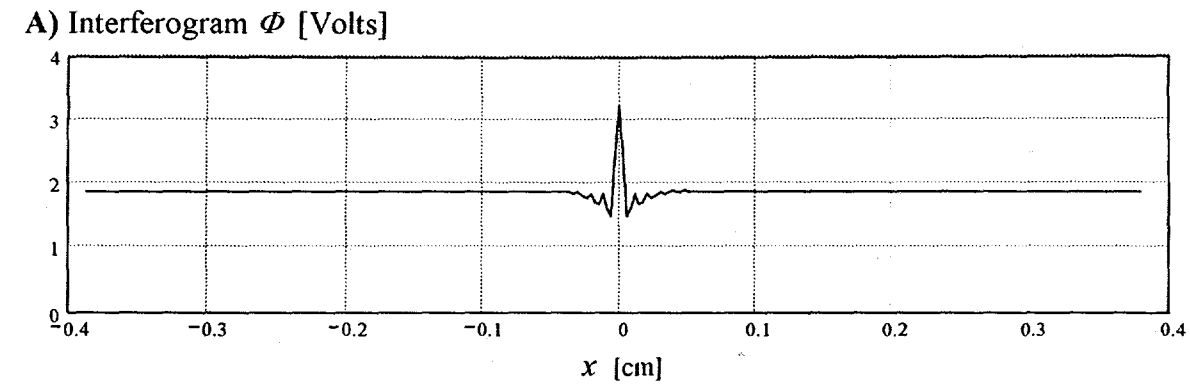

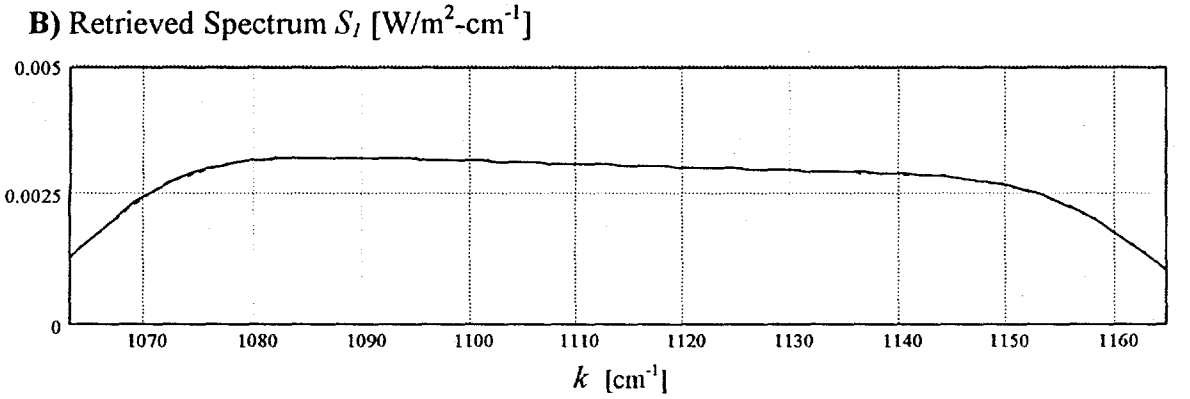

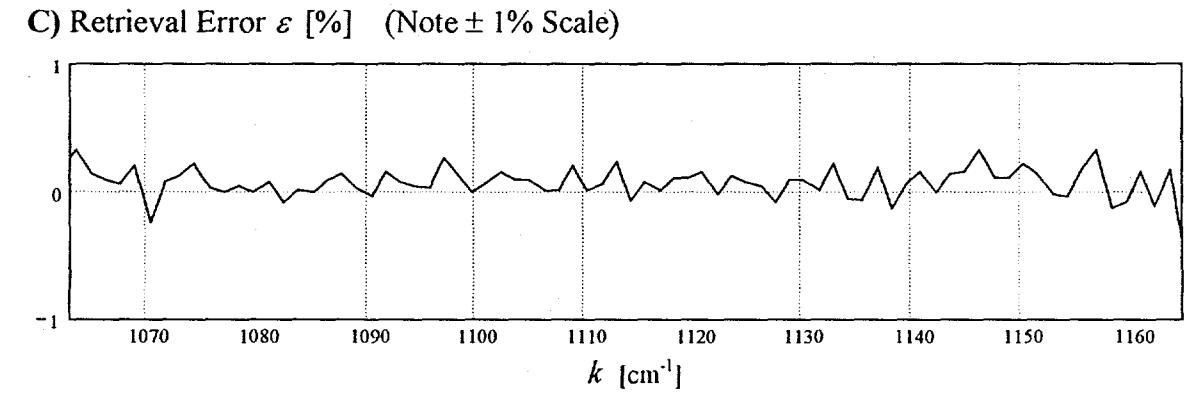

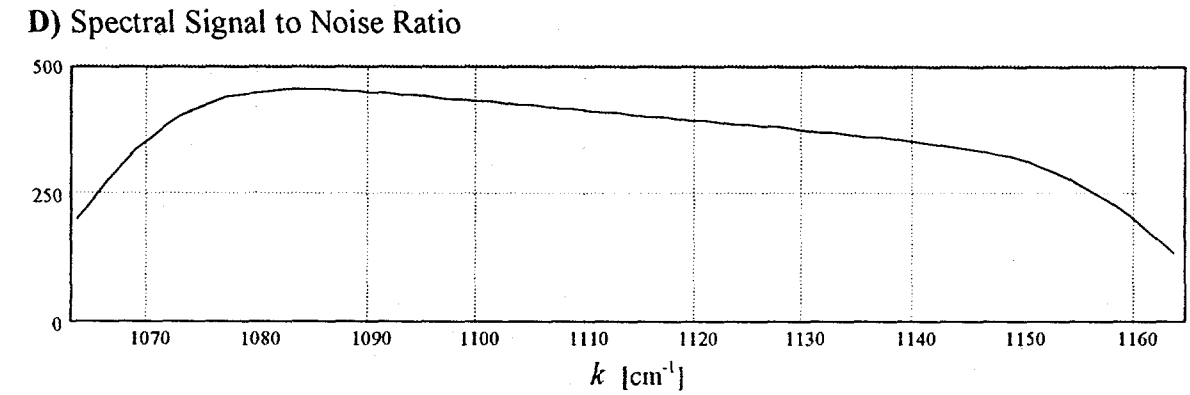

Figure 10. Calibrated response: **A)** Interferogram Φ, **B)** Retrieved spectrum S_I, **C)** Relative retrieval error, and **D)** Spectral signal to noise ratio. Gain and offset non-uniformity are calibrated to 0.01%

System parameters:

- 256x256, 30 μm HgCdTe focal plane array:

  $T_s = 0.1$, sample period (frame rate) [s],
  $\tau_{int} = 0.500 \times 10^{-3}$, integration period [s],
  $G_c = 0.34 \times 10^{-6} q^{-1}$, amplifier conversion gain [V/q],
  $A_d = (30 \times 10^{-6})^2$, detector element (pixel) area [m^2],
  $\Delta f = 5$, noise equivalent bandwidth [Hz],
  $I_d = 0.1 \times 10^{-7}$, detector dark current [A],
  $\eta_d = 0.75$, detection quantum efficiency,
  $\kappa_d = 2$, detection noise factor,
  $v_{n\_a} = 91.6 \times 10^{-6}$, amplifier/read output referred noise voltage [V/√Hz].

- Optics:

  Primary: $D_o = 0.302$ m, $\Delta D_{obs} = 0.35$,
  Effective F#: 2.1
  Pre-interferometer optics: $T_{o\_1} = 0.90$
  Post-interferometer optics: $T_{o\_2} = 0.90$
  Grating Efficiency: $\eta_g = 0.80$
  Filter: $\Delta k = 1063 - 1164$ cm^{-1}, $T_f = 0.80$

- Spectral sources:

  Calibration plate: $T_c = 350$ K, $\varepsilon_c = 1.0$
  Pre-interferometer optics: $T_{op\_1} = 300$ K, $\varepsilon_{op\_1} = 0.05$
  Post-interferometer optics: $T_{op\_2} = 300$ K, $\varepsilon_{op\_2} = 0.10$
  Field-Stop: $T_{fs} = 77$ K, $\varepsilon_{fs} = 1.0$
  Cold-Shield: $T_{cs} = 77$ K, $\varepsilon_{cs} = 1.0$

System simulations for both calibrated and uncalibrated response are shown in **Figures 9** and **10** respectively. A 350 K calibration plate was assumed for a thermal source. Note the strong dependency of the retrieval error given uncalibrated- vs.-calibrated channel gain and offset non-uniformity (defined in **Section 5.3.**).

APPENDIX A: Estimating Transform Noise

- For the quantities $x_n \pm \sigma_n$ $(n = 0,1,2, .. N\text{-}1)$, the function $y = f(x_0, x_1, x_2, \ldots x_{N-1})$ will have a mean error estimated through Gaussian error propagation[27]

$$\sigma_y = \sqrt{\sum_{n=0}^{N-1}\left(\frac{\partial f}{\partial x_n}\right)^2 \sigma_{x_n}^2}\,.$$

- Extending to FTS transform noise, the interferogram samples $\Phi(x_m)\pm\sigma_m$ $(m = 0,1,2, .. N\text{-}1)$ will transform into the spectral domain $S(k_n) = f(\Phi(x_m),k_n)$ where $(m,n = 0,1,2, .. N\text{-}1)$ with a mean error per spectral channel, σ_k ,of

$$\sigma_{k_n} = \sqrt{\sum_{m=0}^{N-1}\left(\frac{\partial f(k_n)}{\partial \Phi(x_m)}\right)^2 \sigma_{x_m}^2}\,.$$

- Substitution of **Equation 25** yields

$$\sigma_{k_n} = hc\,\mathrm{K}\,4\tan(\theta_L)\sqrt{\delta x\sum_{m=0}^{N-1}\left|k_n \Im^{-1}(k_n,x_m)k_n\cos\left(2\pi\left(4\tan(\theta_L)(k_n-k_L)x_m\right)+\theta(k_n,x_m)\right)\right|^2\sigma_{x_m}^2\,\delta x}$$

$[\mathrm{W/m^2\text{-}cm^{-1}}]$.

References

[1] J. Harlander and F. L. Roesler, "Spatial Heterodyne Spectroscopy: A Novel Interferometric Technique for Ground-Based and Space Astronomy," *Proc. SPIE Instrumentation in Astronomy VII*, Vol. 1235, pp. 622-633, 1990.

[2] F. L. Roesler and J. Harlander, "Spatial Heterodyne Spectroscopy: Interferometric Performance at any Wavelength without Scanning," *Proc. SPIE Optical Spectroscopic Instrumentation and Techniques*, Vol. 1318, pp. 234-243.

[3] J. W. Goodman, *Introduction to Fourier Optics*, McGraw-Hill, 1968.

[4] G. O. Reynolds, J. B. DeViles, G. B. Parrent and Brian J. Thompson, *Physical Optics Notebook Tutorials In Fourier Optics*, SPIE and American Institute of Physics, pp. 94-96, 1989.

[5] R. Beer, *Remote Sensing by Fourier Transform Spectrometry*, John Wiley & Sons, 1992.

[6] R. F. Horton, C. A. Conger, and L.S. Pellegrino "High Etendue Imaging Fourier Transform Spectrometer – Initial Results," *Proc. SPIE Imaging Spectrometry III*, Vol. 3118, pp. 380-390, July 1997.

[7] B. W. Smith, B. E. Laubscher, B. J. Cooke, P. LaDelfe, J. M. Harlander, J. W. Howard, and S. Milligan, "The Infrared Imaging Spatial Heterodyne Spectrometer: A New Pushbroom Fourier Transform Ultraspectral Imager with no Moving Parts," *Proc. SPIE Infrared Technology and Applications XXV*, April 1999.

[8] B. W. Smith and J. M. Harlander, "Imaging Spatial Heterodyne Spectroscopy: Theory and Practice," *Proc. SPIE, Infrared Technology and Applications XXV*, April 1999.

[9] G. Waldman and J. Wooton, *Electro-Optical System Performance Modeling*, Artech House, 1993.

[10] *The Infrared Electro-Optical Systems Handbook*, J. S. Accetta and D. L. Shumaker Eds., Information Analysis Center and SPIE Optical Engineering Press, Bellingham WA, Vol. 1 - 8, 1993.

[11] B. J. Cooke, B. E. Laubscher, C. C. Borel, T. S. Lomheim and C. F. Klein "Methodology for Rapid Infrared Multi-Spectral, Electro-Optical Imaging System Performance and Synthesis," *Proc. SPIE Infrared Imaging Systems: Design, Analysis, Modeling, and Testing VII*, pp. 52-86, April 1996.

[12] J. W. Brault, *Fourier Transform Spectroscopy*, A. Benz, M Huber, and M. Mayor Eds., High Resolution in Astronomy: 15th Advanced Course of the Swiss Society of Astronomy and Astrophysics, pp. 1-61, 1985.

[13] A. D. Poularikas, *The Transform and Applications Handbook*, CRC and IEEE Press, 1996.

[14] A. V. Oppenheim, R. W. Schafer, *Digital Signal Processing*, Prentice-Hall, 1975.

[15] J. D. Jackson, *Classical Electrodynamics*, John Wiley & Sons, 2nd Ed., 1975.

[16] S. C. Cohen, "Heterodyne Detection: Phase Front Alignment, Beam Spot Size, and Detector Uniformity," *Applied Optics*, Vol. 14, No. 8, pp. 9153-1958, Aug. 1975.

[17] S. Fowler, G. W. Kamerman, and G. Lawson, "Analysis of Heterodyne Efficiency for Coherent Laser Radars," *SPIE Applied Laser Radar Technology*, Vol. 1936, pp. 137-146, 1993.

[18] J. W. Goodman, Statistical Optics, John Wiley & Sons, 1985.

[19] R. L. Fante, *Signal Analysis and Estimation*, John Wiley & Sons, 1988.

[20] J. Minkoff, *Signals, Noise, & Active Sensors*, John Wiley & Sons, 1985.

[21] A. Papoulis, *Probability, Random Variables and Stochastic Processes*, McGraw-Hill, 1984.

[22] M. S. Keshner, "1/f noise," *Proc. of the IEEE*, Vol. 70(3), pp. 212-218, March 1982.

[23] F. N. Hooge, "1/f noise," *Physica*, Vol. 83B, pp. 14-23, 1976.

[24] J. Vampola, *Readout Electronics For Infrared Sensors, The IR Electro-Optical Systems Handbook*, Vol. 3, SPIE Press, Bellingham WA, 1993.

[25] C. D. Motchenbacher, J. A. Connelly, *Low-Noise Electronic System Design*, John Wiley & Sons, 1993.

[26] S. M. Sze, *Physics of Semiconductor Devices*, John Wiley & Sons, 1981.

[27] H. Bartsch, *Handbook of Mathematical Formulas*, Academic Press, pp. 474 - 476, 1974.